

CAN GEOMETRIC COMBINATORICS IMPROVE RNA BRANCHING PREDICTIONS?

SVETLANA POZNANOVIĆ, OWEN CARDWELL, AND CHRISTINE HEITSCH

ABSTRACT. Prior results for tRNA and 5S rRNA demonstrated that secondary structure prediction accuracy can be significantly improved by modifying the parameters in the multibranch loop entropic penalty function. However, for reasons not well understood at the time, the scale of improvement possible across both families was well below the level for each family when considered separately. We resolve this dichotomy here by showing that each family has a characteristic target region geometry, which is distinct from the other and significantly different from their own dinucleotide shuffles. This required a much more efficient approach to computing the necessary information from the branching parameter space, and a new theoretical characterization of the region geometries. The insights gained point strongly to considering multiple possible secondary structures generated by varying the multiloop parameters. We provide proof-of-principle results that this significantly improves prediction accuracy across all 8 additional families in the Archive II benchmarking dataset.

1. INTRODUCTION

The base pairing of an RNA sequence, i.e. the likely secondary structure(s), provides important molecular information Tinoco, Jr and Bustamante (1999) and can be critical to generating useful functional insights Miao et al. (2020); Schneider et al. (2023); Nithin et al. (2024). The range of RNA secondary structure prediction approaches is large, and ever-expanding as the field pursues continued accuracy improvements. However, the most widely used programs Markham and Zuker (2008); Lorenz et al. (2011); Reuter and Mathews (2010), and their closely related approaches, are based on optimizing a “free energy” score under the nearest neighbor thermodynamic model (NNTM).

Under the NNTM, a secondary structure decomposes into well-defined substructures, e.g. a stack of two consecutive bases pairs or a hairpin loop closed by a single pair. Each substructure is assigned a score based on the model parameters. These values are then summed to generate the NNTM score, called the “folding free energy change” and denoted ΔG , for the whole structure. It is worth emphasizing that this ΔG number is an *approximation* to the actual physiochemical quantity of energy that would be released were the full sequence somehow folded in vitro. Nonetheless, calculating the minimum free energy (MFE) score for a sequence, and an associated secondary structure, can yield very useful information. This is particularly true when multiple possible “suboptimal” structures are considered rather than just a single prediction.

A secondary structure for the given RNA sequence is called suboptimal if its ΔG value is close to the MFE score under the current NNTM evaluation. It has long been recognized that prediction accuracy improves when these alternative structures are also considered Mathews (2006); Rogers and Heitsch (2016). For instance, the three different NNTM parameterizations Jaeger et al. (1989); Mathews et al. (1999, 2004) have always reported a “best suboptimal” accuracy which can be understood as an indicator of the approximation quality. On average over the set of sequences tested Mathews et al. (1999), the most accurate suboptimal structure found (among up to 750 alternative predictions) had a ΔG score within 4.8% of the MFE. Hence, NNTM optimization — particularly when alternative predictions are also considered — captures crucial RNA base pairing information.

It is worth considering how suboptimal structures can be generated. Stochastic sampling from the Boltzmann distribution McCaskill (1990); Ding and Lawrence (2003) is the current standard. However, this approach magnifies small differences in the NNTM score since the Boltzmann probability is exponential in the ΔG values. Historically, there have been other approaches, including deterministic sampling Zuker (1989) and exhaustive generation Wuchty et al. (1999), which can produce a broader range of alternative predictions. This can be important when the sampled structures are the basis for further analysis. For instance, structural variety is a crucial characteristic in recent results Entzian et al. (2021) motivated by RNA folding kinetics.

We provide here a *mathematical* motivation for generating alternative predictions based on a parametric analysis of RNA branching Drellich et al. (2017); Barrera-Cruz et al. (2018); Poznanović et al. (2020, 2021). Using methods from geometric combinatorics Drellich et al. (2017), it is possible to identify

all optimal predictions under any parameterization of the entropic branching penalty. However, due to rapid growth in branching polytope complexity with sequence length, only two types were considered: transfer RNA (tRNA) and 5S ribosomal RNA (rRNA). We demonstrated Poznanović et al. (2020) that re-parameterizing the linear penalty for multiloop initiation can significantly improve the MFE prediction accuracy on a set of 100 sequences, evenly split between the two families. New parameter combinations were obtained by intersecting large cliques in pairwise compatibility for the most accurate predictions. Perplexingly, however, the combinations that were better for tRNA were worse for 5S rRNA, and vice versa.

To determine the exact amount of improvement possible on the whole set, as well as each family, a branch-and-bound algorithm was developed Poznanović et al. (2021). The new results confirm the ‘exclusive disjunction’ conundrum; re-parameterizing over the whole set yields an average prediction accuracy of 0.66 versus 0.54 for the Turner 2004 Mathews et al. (2004); Turner and Mathews (2010) parameters. However, parameterizing tRNA alone improves their accuracy from 0.45 to 0.75, and from 0.64 to 0.73 for just 5S rRNA. Moreover, the conclusion that the best prediction accuracy via branching re-parameterization is an ‘either-or-but-not-both’ situation for these two families was validated by testing the new parameters on the large number of tRNA and 5S rRNA sequences in the Archive II benchmarking dataset Sloma and Mathews (2016); Mathews (2019) from the Mathews Lab (U Rochester). Finally, to further confound the situation, parameter combinations which seem numerically ‘far’ from each other can generate statistically indistinguishable accuracies, even on the small training set of 100 sequences. This makes the choice of a single ‘best’ parameter combination seem rather arbitrary.

Here these incongruities are resolved by careful consideration of the parameter region geometry. Preliminary visual inspection had suggested that, for each family, the regions corresponding to the target conformations — a Y-shape for 5S rRNA and a cloverleaf for tRNA — had a characteristic shape, size, and location. Moreover, these two sets seemed to be largely disjoint from each other. If confirmed, this would reconcile the potential for improving accuracy within a family with the challenge for achieving the same level of improvement between the two families.

Furthermore, although the shape and approximate location were maintained under a dinucleotide permutation of each sequence, the region size shrank considerably. This suggested that the former are somehow intrinsic to the NNTM optimization while the latter is particular to the biological sequences. Specifically, the unusually large region size suggests a robustness/stability of the family-specific branching conformation.

The results here confirm these initial insights. This was achieved through two methodological advances. First, we present a reduced polytope algorithm which leverages the existing code base to more directly compute the parameter slice of interest. The reduction in geometric complexity, and therefore compute time, makes rigorous randomized comparisons tractable for the first time. Second, we introduce a linear transformation of the parameter space which illuminates the underlying geometry. In this context, we characterize the general shape, and give explicit formulas for the size and midpoint location, for the two parameter regions of interest. We then use these two advances to give a thorough analysis of the geometric characteristics of the 100 training sequences in comparison to a large number (12,000 per family) of random counterparts.

We confirm that the size of the family-specific target regions is extreme. In sharp contrast to the random sequences, the biological ones almost always have a target branching conformation that is optimal under a range of parameters that is typically 4.47 times larger for 5S rRNA and 26.33 times for tRNA. This size, and the consistency in their midpoint locations, explains how a non-empty intersection can be found for almost all 50 sequences when each family is considered separately. However, when considered together, the pairwise overlaps between the different target regions are too variable to resolve into a comparable cumulative intersection. This explains the impossibility of achieving the same level of prediction accuracy between families as within them.

Given that this parameter geometry is intrinsic to the NNTM optimization, we propose working with — rather than against — its either-or-but-not-both consequences. In particular, we explore the potential for improving prediction accuracy by considering ‘suboptimal’ structures generated by varying the branching parameters. In other words, we consider a range of possible linear approximations for the multiloop entropic penalty. The proof-of-principle results for these alternative predictions are quite promising. Not only does such an approach achieve the highest accuracy thus far on the tRNA and 5S rRNA training family counterparts in the Archive II dataset, but it significantly improves the accuracy for all 8 other families as well.

2. BACKGROUND

2.1. NNTM parameterization. The quality of the NNTM approximation is fundamentally dependent on the parameters used to score the substructures. Recall that there have been three major versions Jaeger et al. (1989); Mathews et al. (1999, 2004), referred to as the Turner 1989 (T89), Turner 1999 (T99), and Turner 2004 (T04) sets. The ‘modern’ T99 and T04 values are available online through the nearest neighbor database (NNDB) Turner and Mathews (2010). For comparison, the ‘historic’ T89 ones can also still be accessed¹ online.

Different aspects of the NNTM are recognized as more or less well-determined. The most reliable are the ΔG values for the 21 distinct base pair stacks. They are firmly grounded in experimental data Freier et al. (1986); Xia et al. (1998), and did not change from T99 to T04. At the other extreme, the standard form for the branching entropic penalty (discussed in detail below) is typically regarded as “ad-hoc” at best Ward et al. (2017), and involves three parameters which have changed substantially with each new version.

In between these extremes are the large number of parameters for all the other components of the NNTM: the dangling ends and terminal mismatches as well as the hairpin, bulge, internal, and external loop scores. For instance, the ‘small’ internal loops, i.e. the ones containing two base pairs and having 1×1 , $1 \times 2/2 \times 1$, or 2×2 single-stranded bases on each side, were introduced in T99. They have more than 7,000 parameters among them, accounting for the 5’ – 3’ symmetry. These parameters were updated for T04 based on new experimental data (see citations in Mathews et al. (2004)). The authors indicate that...

“... measured values are used when available for 1×1 , 1×2 , and 2×2 internal loops, but approximations are used for most internal loops. The range of measured free energies differs for different types of internal loops. For example, the range is roughly 2 and 6 kcal/mol for 1×3 (*sic*) and 2×2 loops, respectively. Evidently, different types of loops require different approximations.”

The NNTM approximation for multibranch loops (also known as junctions or multiloops) has two components: an initiation term, which is understood as an entropic penalty, and a stacking term for the favorable intra-loop interactions. In principle Turner and Mathews (2010), the stacking term is “the optimal configuration of dangling ends, terminal mismatches, or coaxial stacks, noting that a nucleotide or helix end can participate in only one of these favorable interactions.” In practice, the extent to which these stacking interactions are part of the NNTM optimization can vary. For instance, RNAfold Lorenz et al. (2011) has four different dangling end options, and the default allows “a single nucleotide to contribute with all its possible favorable interactions.” This approximation, known as the “d2” option², facilitates efficient partition function calculations but definitely can alter the MFE score, and hence the accompanying structural prediction.

The standard form for the initiation term/entropic penalty is:

$$\Delta G_{\text{init}} = a + b \cdot [\text{number of unpaired nucleotides}] + c \cdot [\text{number of branching helices}]$$

for branching parameters (a, b, c) whose values have changed considerably over time:

$$\text{T89} = (4.6, 0.4, 0.1) \quad \text{T99} = (3.4, 0, 0.4) \quad \text{T04} = (9.3, 0, -0.6).$$

We particularly note the substantial increase in a and the negative c value in the T04 parameters, as well as that $b = 0$ in both T99 and T04.

It is critical to appreciate that the T89 and T99 ones were *learned*, i.e. they were derived by maximizing the MFE prediction accuracy over a set of known structures. In contrast, the current T04 values are based on experimental data from small model systems Diamond et al. (2001); Mathews and Turner (2002). There is, however, an important caveat. The optical melting data was used to parameterize a different function, where the term involving b above is replaced by $b' \cdot [\text{average asymmetry}]$ with $b' = 0.91 \pm 0.19$. However Mathews et al. (2004), this term is “neglected” since the average asymmetry computation “cannot be accommodated in a dynamic programming algorithm.” Effectively, then this more accurate model is reduced to the simple linear one with $b = 0$.

Recall that the linear penalty function was originally introduced for computational efficiency Jaeger et al. (1989); Zuker et al. (1999). However recent results Ward et al. (2017) have demonstrated that it

¹Via the Internet Archive Wayback Machine as “Version 2.3 free energy paramters for RNA folding” at <http://www.bioinfo.rpi.edu/~zukerm/cgi-bin/efiles.cgi?T=37>. The T99 set was originally called “Version 3.0”.

²For completeness, the `pmfe` code Drellich et al. (2017) was based on `Gfold` Swenson et al. (2012) which implemented the common dangling options at that time. The `pmfe` default, which has been used for all parametric analysis results thus far, corresponds to RNAfold’s “d1” option, although d2 is also implemented.

out-performs both the logarithmic penalty Mathews et al. (1999) based on Jacobson–Stockmayer theory and also one based on polymer theory Aalberts and Nandagopal (2010). From this the authors conclude that “the simplest model is best.”

Interestingly, their results included re-parameterizing the logarithmic and the polymer models, since some of the original values were learned using the T99 parameters for the rest of the NNTM. Their 40 sequence training set was evenly split between tRNA and 5S rRNA. They found that the newly optimized parameters for both models...

“...improve performance for tRNA, but not for 5S rRNA. This is unexpected, as an equal number of tRNA and 5S rRNA were used for training. Looking at the performance of the parameters on a per RNA basis in the training set suggests that either the performance on tRNA could be increased, or the performance on 5S rRNA could be increased, but not both. We hypothesize that this means that the models themselves are insufficient to describe the space of multi-loop free energies completely.”

2.2. Parametric Analysis. In recent work, tools from geometric combinatorics were useful in performing a complete parametric analysis and quantifying the robustness of the minimum free energy (MFE) prediction as the branching parameters are changed Poznanović et al. (2020). The analysis showed that improvement of the prediction for multiple families is possible but difficult because competing parameter combinations favor different families Poznanović et al. (2021). Whereas previous results focused on isolated parameter combinations, here we explicitly consider the regions of equivalent parameters which yield the same optimal structure. Each of the regions considered yields a structure with a distinct branching pattern. We show that for each of the families, the target branching region has a characteristic geometry which is different from that of the other.

Previous work Drellich et al. (2017) introduced a formulation of the MFE prediction as a linear program focusing on the branching characteristics. In particular, the *branching signature* of an RNA secondary structure S was defined to be a quadruple (x, y, z, w) where x , y , and z are the total number, respectively, of multibranch loops (a.k.a. junctions) as well as of single-stranded bases and of helices in those loops, and w is the residual free energy from all the other structural components. The first three correspond to the cumulative number, size, and complexity of the predicted branch points.

$$\Delta G(S) = ax + by + cz + dw, \quad (1)$$

where a , b , and c are the standard components of the NNTM multiloop initiation and d is a scaling term to complete the linear program. Because of this, using methods from geometric combinatorics — specifically convex polytopes and their normal fans — it is possible to give a complete analysis of the effect that the branching parameters have on determining the optimal secondary structure.

The `pmfe` code introduced in Drellich et al. (2017) finds all vertices of the *branching polytope* for the given RNA sequence. Each vertex is a branching signature which minimizes Eq. (1) for some set of real values (a, b, c, d) . The polytope’s normal fan is then a conic subdivision of the 4d parameter space with maximal cones containing all parameters that yield the same optimal signature. In the NNTM model, the last parameter d is fixed at 1, and hence a parametric analysis need only analyze the $d = 1$ slice of this normal fan. In this way, we find the optimal signatures, and their associated secondary structures, for every combination of possible NNTM branching parameters.

In Poznanović et al. (2020), this geometric combinatorics approach gave a complete analysis of the prediction accuracy, stability, and robustness for a diverse set of 50 tRNA and 50 5S rRNA sequences. By analyzing all possible optimal secondary structures for each sequence, we found that every one had a high accuracy prediction for some combination of $(a, b, c, 1)$ values. However, it was not possible to achieve this level of improvement for all sequences with the same parameter triple — not even within the same family.

Subsequently, a branch-and-bound algorithm Poznanović et al. (2021) showed that there exist parameters that significantly improve prediction accuracy for the tRNA test sequences and other combinations that work for the 5S rRNA ones. Moreover, the best possible improvement over both families simultaneously is significantly lower. These conclusions were tested against a much larger dataset (Archive II), and found to remain valid. Hence, it was well-understood that changing the default NNTM branching parameters can significantly improve secondary structure prediction accuracy, but not why different combinations are required for tRNA and for 5S rRNA.

To resolve this question, it was determined to focus on the $b = 0$ slice of the $d = 1$ normal fan hyperplane. This agrees with the current NNTM branching parameters and is supported by results Poznanović et al. (2021) showing that different b values near zero have equivalent maximum accuracy improvements.

Moreover, it allows to focus clearly on the geometry of the optimal parameter regions in the (a, c) plane, particularly the two which correspond to the target branching signatures for tRNA and for 5S rRNA. We find large overlap in the target region parameters within each family, but that these family-specific values occupy essentially distinct parts of the parameter space from each other. Furthermore, we show that this region geometry is a true biological signal by comparison with a large randomized dataset.

Since computing the branching polytope for the sequence lengths we consider takes several hours, we develop an algorithm for computing the $b = b_0, d = 1$ slice for any fixed value b_0 and use it to generate our data. Our algorithm leverages the existing code but computes the desired slice without computing the branching polytope. We show that the location and geometry of the target regions depend on the differences of the residual energies corresponding to structures to close branching patterns and we give exact formulas for the target branching of tRNA and 5S rRNA sequences. Analysis of the distributions of the differences explains the previously observed large overlap of the same target regions for the homologous sequences. Moreover, results show that the target regions are present with higher frequency and bigger area for the biological sequences compared to random ones. We give details about which differences of residual energies have the biggest effect on the difference in the geometry of the regions. Finally, based on the insights from the data analysis, we consider secondary structure prediction by generating multiple structures which correspond to branching parameters in the neighborhood of the target regions for tRNA and 5S RNA. We show that if the (a, c) branching parameters are allowed to vary over a relatively small region, we get a measurable increase in the prediction accuracy for all additional families in the Archive II benchmarking data set.

3. METHODS

3.1. Algorithm for slice computation. An RNA secondary structure refers to the base-pairing interactions within a single RNA molecule, which gives rise to specific shapes or motifs: helices made of stacked base pairs separated by different types of loops (bulges, internal and hairpin loops, and junctions). The junctions are regions where 3 or more helices converge. Recall that the signature of an RNA secondary structure is the quadruple (x, y, z, w) where x, y , and z are the total number, respectively, of junctions, single-stranded bases and helices in those loops, and w is the residual free energy from all the other structural components. For a given RNA sequence s , its branching polytope P_B is the convex hull of the set of signatures that correspond to secondary structures over s . For a face F of a polytope P , its corresponding normal cone is the set of all vectors \mathbf{A} such that any point $\mathbf{v} \in F$ minimizes the product $\mathbf{A}\mathbf{v}$. The normal fan of a polytope P is the collection of its normal cones and is denoted by $\mathcal{N}(P)$. The full dimensional cones of $\mathcal{N}(P)$ correspond to the vertices of P .

Recall that d is a “dummy” parameter introduced to complete the linear program, and only biologically relevant when $d = 1$. The $d = 1$ slice of $\mathcal{N}(P_B)$ is a subdivision of the a, b, c - parameter space in convex regions, so that branching parameters from the same region yield the same optimal branching signature. For our data analysis, we also specialize $b = 0$, which is consistent with both the prior T99 and current T04 branching parameters.

Prior results had characterized the infinite regions theoretically Barrera-Cruz et al. (2018) and both types computationally Poznanović et al. (2020). It was shown that the cones are quite “thin” in the b dimension Poznanović et al. (2020), but also that this does not make a statistically significant difference to the prediction accuracy Poznanović et al. (2021). In other words, although individual predictions are not necessarily robust to small changes in b , there are (a, c) values with equivalent accuracy on average whether $b \leq 0$ or $b \geq 0$.

In this section we describe an algorithm for computing the $b = b_0, d = 1$ slice (from now on a b_0 -slice) of $\mathcal{N}(P_B)$, for a fixed value $b_0 \in \mathbb{R}$, which leverages the existing code for polytope computation but avoids computing P_B itself. The flow of the algorithm is represented in Figure 1. It uses the same main components used in the `pmfe` Drellich et al. (2017) branching polytope calculations with some modifiers. In particular, the `iB4e` module we use is an adaptation of the software developed by Huggins Huggins (2006). In our case, this module internally incrementally builds a 3d polytope, denoted in the explanation below by P_3 , by extending it in various directions as in the Beneath-and-Beyond algorithm Grünbaum et al. (1967). The main idea behind the Beneath-and-Beyond algorithm is to build a desired polytope by starting with a small initial approximation and then try to confirm the facets of the approximation by checking that there are no vertices ‘beyond’ it. When a new vertex is found (and thus the confirmation of the facet fails), it is used to refine the approximation.

The polytope P_3 that our algorithm builds internally is the image of the branching polytope P_B under the transformation $T : \mathbb{R}^4 \rightarrow \mathbb{R}^3$ given by

$$T(\mathbf{v}) = \begin{bmatrix} 1 & 0 & 0 & 0 \\ 0 & 0 & 1 & 0 \\ 0 & b_0 & 0 & 1 \end{bmatrix} \mathbf{v}$$

and is not output to the user. While P_3 is not output itself, the algorithm outputs signatures which are preimages of the vertices of P_3 . We denote the convex hull of those signatures by P_4 . The steps of the algorithm are illustrated in Figure 1 and the arrows refer to the following steps:

- (a) Each time **iB4e** tries to confirm a facet of P_3 , it outputs a vector $\mathbf{p} = (a, c, d)$.
- (b) The **find-mfe** module finds an MFE structure for the vector $\mathbf{p}' = (a, b_0d, c, d)$.
- (c) The **scorer** module finds the (x, y, z, w) signature of the MFE structure.
- (d) The vector $(x, z, w + b_0y)$ is passed back to **iB4e** to either confirm the facet with normal \mathbf{p} or to extend P_3 by a new vertex.
- (e) If the facet is not confirmed, (x, y, z, w) is stored in the .rnapoly file.

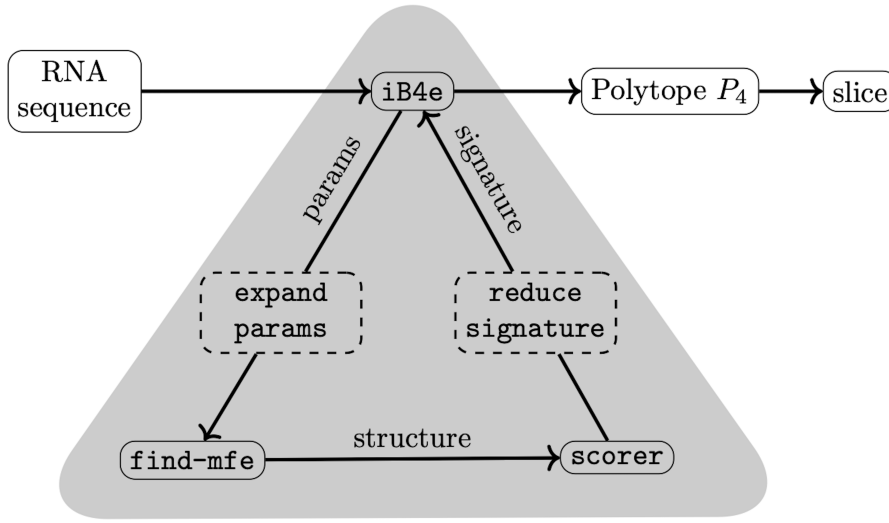


FIGURE 1. Control flow of computing the b_0 -slice of $\mathcal{N}(P_B)$. The dashed boxes represent modifications introduced to the algorithm for computing the branching polytope P_B Drellich et al. (2017).

The final .rnapoly file contains points whose convex hull is a 4d polytope P_4 .

Theorem 1. *The polytope P_4 has the property*

$$\mathcal{N}(P_B) \cap \{b = b_0, d = 1\} = \mathcal{N}(P_4) \cap \{b = b_0, d = 1\}.$$

Proof. Since

$$(a, b_0d, c, d) \cdot (x, y, z, w) = ax + cz + d(w + b_0y),$$

the vertices of P_4 correspond to MFE minimization by vectors (a, b_0d, c, d) for all triples (a, c, d) by construction. Let (a', c') be in the b_0 -slice of $\mathcal{N}(P_4)$. Then $(a', b_0, c', 1)$ is in $\mathcal{N}(P_4)$ corresponding to a signature (x, y, z, w) , which means (a', c') is in the b_0 -slice of $\mathcal{N}(P_B)$ corresponding to the same signature. Therefore,

$$\mathcal{N}(P_4) \cap \{b = b_0, d = 1\} \subseteq \mathcal{N}(P_B) \cap \{b = b_0, d = 1\}.$$

The converse inclusion follows similarly. \square

The complexity of the Beneath-and-Beyond algorithm for constructing a polytope is $O(V + F)$, where V is the number of vertices and F is the number of facets of the polytope being computed (since the objective vectors are chosen so that after each iteration, either a new vertex of the convex hull is found or a facet of the convex hull is confirmed the method requires running the LP solver for no more than $O(V + F)$ objective vectors). Compared to P_B , the new polytope P_4 has a significantly fewer number of vertices and facets. This results in significantly faster computations of the desired slice. Including the step required to construct a polytope object that can be analyzed (for this we used **SageMath** The Sage Developers

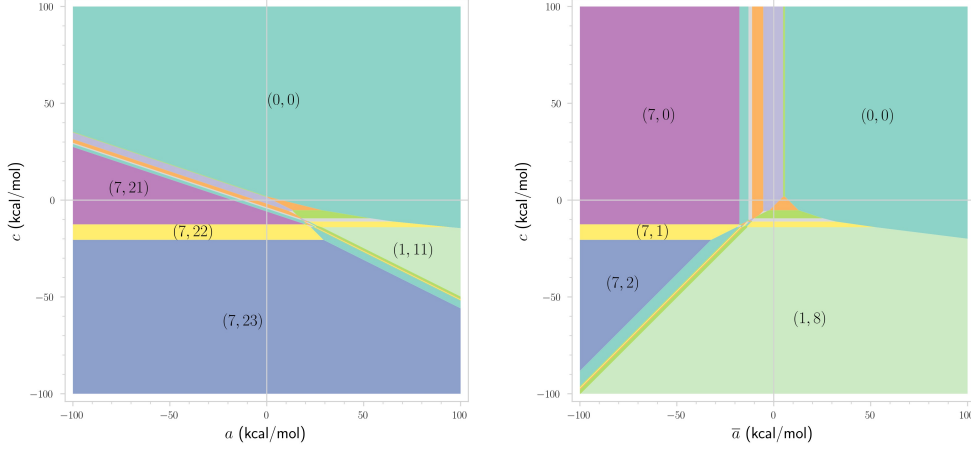


FIGURE 2. The excess branching transformation is illustrated by two $b = 0$, $d = 1$ parameter slices for a biological tRNA sequence. Corresponding regions are colored the same, and larger ones are labeled with the appropriate reduced signature. For example, the (7,21) purple triangle in the original (a, c) plane on the left is transformed into the (7,0) rectangle in the (\bar{a}, c) plane on the right. The parameter range used is only to illustrate the mathematical transformation, and certainly not biologically meaningful.

(2020)), the computation time reduced from ~ 50 min to ~ 83 s for tRNA and from ~ 11 h to ~ 8 min for 5S rRNA. The code for computing a b_0 -slice is available at: <https://github.com/gtDMMB/pmfe2023>.

3.2. Slice geometry. We consider the normal fan associated with an RNA branching polytope, and investigate finite regions in the two-dimensional slice obtained by specializing the b and d parameters. As with the previous algorithmic results, the transformation of the parameter space is presented for an arbitrary b_0 -slice, i.e. the (a, c) plane obtained for any fixed $b = b_0$ (and $d = 1$). We then characterize the regions corresponding to the target branching signatures for tRNA and 5S rRNA, focusing on the geometry for $b = 0$.

3.2.1. Excess branching formulation of linear program. We begin by reformulating the optimization to better illuminate the slice geometry. Since every junction must contain at least three helices, $z = 3x + \bar{z}$ where the new variable $\bar{z} \geq 0$ denotes the total ‘excess’ branching beyond the $3x$ minimum. Then

$$(a, b_0, c, 1) \cdot (x, y, z, w) = (\bar{a}, b_0, c, 1) \cdot (x, y, \bar{z}, w)$$

where the new parameter $\bar{a} = a + 3c$ is the minimum penalty per junction.

As seen in Figure 2, this transformation eliminates the $1/3$ skew in the original (a, c) plane. Results from Barrera-Cruz et al. (2018) — appropriately reinterpreted — still hold. As before, all sequences have a unique region $(0, 0, 0, w_0)$ with the minimum number of junctions, the minimum (total or excess) branching, and the minimum residual free energy w_0 over all such structures. This infinite region always dominates the upper-right quadrant.

There is at most one optimal region with a given number of junctions and branches in each b_0 -slice. Call these two values the reduced signature for that region, and denote the region as $R_{x,z}$ or $R_{x,\bar{z}}$ as appropriate. In the (a, c) plane, adjacent $R_{x,z}$ and $R_{x',z'}$ are separated by a horizontal line if and only if $x = x'$. This remains true in (\bar{a}, c) . Moreover, now the dual holds as well; adjacent regions $R_{x,\bar{z}}$ and $R_{x',\bar{z}'}$ are separated by a vertical line if and only if $\bar{z} = \bar{z}'$.

There is a maximum number of junctions, denoted x_{max} , over the branching polytope. We assume $x_{max} > 0$, which holds except for extreme cases (such as GGGGCCCC) which have no possible structures containing any junctions.

There is always an infinite region $(1, \bar{z}_{max}(1))$, that is a region where the number of excess branches for the single junction is the largest possible over the entire polytope. This now dominates the lower (\bar{a}, c) half-plane pictured in Figure 2. It is adjacent to $(0, 0)$ since crossing a region boundary moving horizontally to the right must decrease x . Likewise, moving vertically upward must decrease \bar{z} if a boundary is crossed. The slope of the boundary is determined by what happens to the other variable. In particular, if regions (x, y, \bar{z}, w) and (x', y', \bar{z}', w') are adjacent, then their boundary line in the b_0 -slice is

$$\Delta_x \bar{a} + \Delta_{\bar{z}} c = -\Delta_y b_0 - \Delta_w$$

for $\Delta_x = x - x'$, etc.

Since an excess branch can always be removed from a structure, there exist reduced signatures (not necessarily optimal) for $(1, \bar{z})$ with $0 \leq \bar{z} \leq \bar{z}_{\max}(1)$. When these signatures are optimal, they dominate the finite regions in the b_0 -slice and form the left boundary of $R_{0,0}$.

When there exists a signature $(x_{\max}, y, 0, w)$, that is when $\bar{z}_{\min}(x_{\max}) = 0$, then the other infinite regions in the upper half-plane are vertical ‘strips’ $(x, 0)$ with $0 < x < x_{\max}$. This is true for all polytopes analyzed here, but can fail for sufficiently pathological³ sequences.

The other infinite regions in the lower-half plane are $(x_{\max}, \bar{z}_{\max}(x_{\max}))$, whose skewed version dominates the (a, c) one, and a progression of $(x_i, \bar{z}_{\max}(x_i))$ with $1 = x_0 < x_1 < \dots < x_{\max}$. As with the vertical strips in the upper half-plane, the x values are not necessarily contiguous. While the slope of their boundary lines is often 1, smaller values are not uncommon⁴ for biological sequences. Finally, if there is an (x_{\max}, \bar{z}) region with $\bar{z}_{\min}(x_{\max}) < \bar{z} < \bar{z}_{\max}(x_{\max})$, then this will be a horizontal infinite ‘strip’ as with the $(7, 22)/(7, 1)$ one in Figure 2.

3.2.2. Characterizing tRNA and 5S rRNA target regions. The reduced excess branching signature for the classic tRNA cloverleaf secondary structure is $(1, 1)$, while the Y-shape 5S rRNA one is $(1, 0)$. We refer to these as the target region for the respective family. We will show that their geometry typically displays a clear biological signal, as pictured in Figure 3, in contrast to the randomized comparisons. For clarity, the results are presented for $b = 0$, but it is straightforward to generalize to arbitrary $b_0 \neq 0$.

As seen in Figure 3, it is possible to have a b_0 -slice with $R_{1,0}$ but not $R_{1,1}$ and vice versa. In general, many of the random sequences have both and some neither. If a target region exists, then its right boundary is always $R_{0,0}$. The left boundary is $R_{k,0}$ for $k > 1$ and bottom is $R_{1,j}$ where $j \geq 1$ for $R_{1,0}$ and $j \geq 2$ for $R_{1,1}$. If these are the only boundaries, then $R_{1,0}$ is an (infinite) rectangle and $R_{1,1}$ a triangle. If $R_{1,1}$ is bounded above by $R_{1,0}$, then it’s a trapezoid.

We note that the lower left corner of the target region can have additional boundary edges. For simplicity, however, we do not consider those in our area approximation. We show in Section 4.4 that the geometric formulas below are a very good approximation to the area and location of the target regions. Moreover, this permits us to explicitly consider the different residual energy factors, and determine which is the strongest biological signal.

We first give the geometry approximation for the $(1, 0)$ region. Assume that $R_{1,0}$ exists and is bounded only by $R_{0,0}$ on the right, $R_{k,0}$ for $k > 1$ on the left, and $R_{1,j}$ for $j \geq 1$ on the bottom. Then the boundary lines are

$$\bar{a} = (w_{0,0} - w_{1,0}) \quad (2)$$

$$\bar{a} = \frac{(-1)(w_{k,0} - w_{1,0})}{k - 1} \quad (3)$$

$$c = \frac{(-1)(w_{1,j} - w_{1,0})}{j}. \quad (4)$$

Denote these three values as $\delta_0(0, 0)$, $\delta_0(k, 0)$, and $\delta_0(1, j)$ respectively. Then the width of $R_{0,0}$ is $\delta_0(0, 0) - \delta_0(k, 0)$. The region is unbounded above, so we compute the height as $c_0 - \delta_0(1, j)$ where $c_0 = \max_D \{\delta_0(1, j)\} + 0.1$ with D being the entire dataset considered. The midpoint coordinates (a_m, c_m) are then the averages of the two bounding line values. When $k = 2$ and $j = 1$, this reduces to $\frac{1}{2}(w_{0,0} - w_{2,0}, c_0 + w_{1,0} - w_{1,1})$.

Now, we consider the geometry approximation for the $(1, 1)$ region. The assumptions for $R_{1,1}$ are essentially the same. Suppose further that $R_{1,0} = \emptyset$. Then the right, left, and bottom boundary lines are, respectively,

$$c = (-1)\bar{a} + (w_{0,0} - w_{1,1}) \quad (5)$$

$$c = (k - 1)\bar{a} + (w_{k,0} - w_{1,1}) \quad (6)$$

$$c = \frac{(-1)(w_{1,j} - w_{1,1})}{(j - 1)} \quad (7)$$

³For instance, GGGAAACGAAACCGGAAACGAAACCGGAAACGAAACCC has $x_{\max} = 4$ but $\bar{z}_{\min}(x_{\max}) = 1$ while for $\bar{z}_{\min} = 0$, $x_{\max}(\bar{z}_{\min}) = 3$. We also note that $z_{\max}(x_{\max})$ is not always z_{\max} , e.g. GGGAAACGAAACGAAACCGGAAACGAAACGAAACGAAACCC has $x_{\max} = 4$ and $z_{\max} = 13$ but $x_{\max}(13) = 3$ and $z_{\max}(4) = 0$.

⁴Previously Barrera-Cruz et al. (2018), we had noted that ACCCGGACCCUUUCCAGCCCA violates the common progression $\bar{z}_{\max}(x) \leq \bar{z}_{\max}(x - 1) - 1$ since $\bar{z}_{\max}(2) \geq 0$ but $\bar{z}_{\max}(1) = 0$. The progression holds when the $\bar{z}_{\max}(x)$ structure is “planted,” i.e. has an external loop with only one branch.

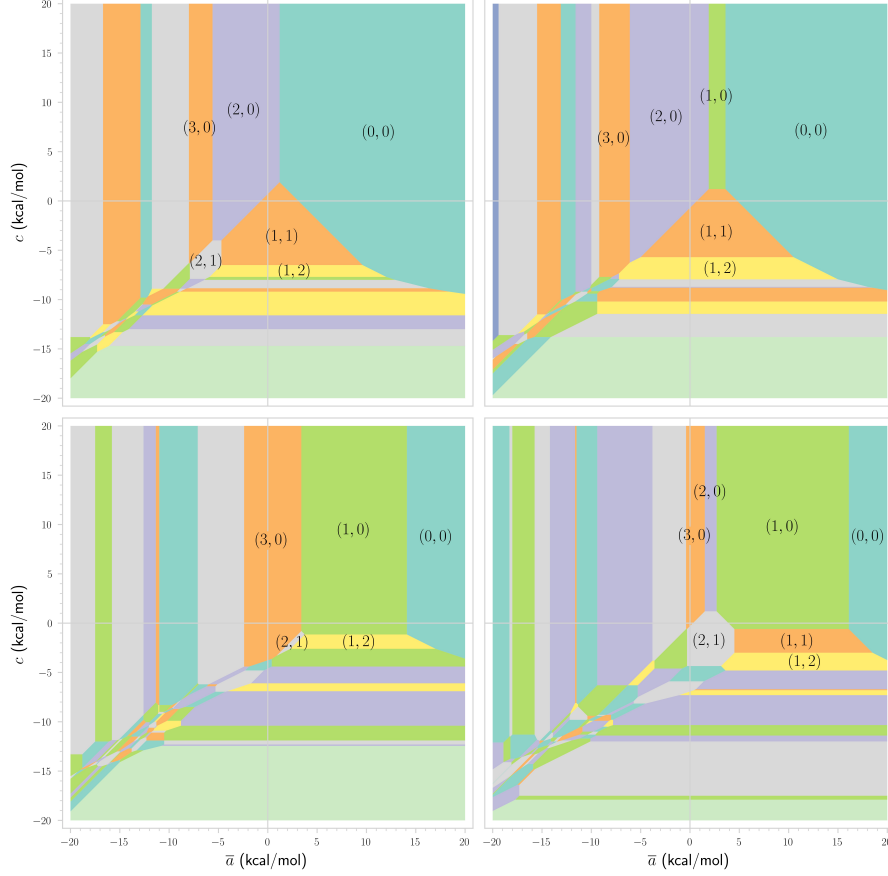


FIGURE 3. Four $(\bar{a}, 0, c, 1)$ slices with regions colored consistently. The upper two are tRNA sequences, and exhibit the characteristic large (orange) triangle/trapezoid with reduced signature $(1, 1)$. The lower two are 5S rRNA, and have the expected large (green) rectangle for the $(1, 0)$ region. Within the two families, the size and location of their target region is quite consistent. However, the first tRNA has no $(1, 0)$ region, and the second has a more typical width. Likewise, the first 5S rRNA has no $(1, 1)$ region, and the second has a more typical height.

and form a triangle T in the (\bar{a}, c) -plane with apex

$$\left(\frac{w_{0,0} - w_{k,0}}{k}, \frac{w_{k,0} + (k-1)w_{0,0}}{k} - w_{1,1} \right). \quad (8)$$

Let $\delta_1(k, 0) = \frac{1}{k}(w_{k,0} - w_{1,1})$, $\delta_1(0, 0) = \frac{k-1}{k}(w_{0,0} - w_{1,1})$, and $\delta_1(1, j)$ be the value from Equation 7. Then the height of T , denoted h_T , is $\delta_1(k, 0) + \delta_1(0, 0) - \delta_1(1, j)$ and its area is $\frac{k}{2(k-1)}h_T^2$.

If instead $R_{1,0} \neq \emptyset$, then $R_{1,1}$ is a trapezoid whose top boundary is $c = w_{1,0} - w_{1,1}$. Denote this value as $\delta_1(1, 0)$. The trapezoid's area is $\frac{k}{2(k-1)}(h_T^2 - h_t^2)$ for

$$h_t = \frac{1}{k}(w_{k,0} - w_{1,0}) + \frac{k-1}{k}(w_{0,0} - w_{1,0}) = \frac{k-1}{k}(\delta_0(0, 0) - \delta_0(k, 0)). \quad (9)$$

Hence, the area of $R_{1,1}$ is a function of up to five weighted energy differences.

We compute the midpoint coordinates (a_m, c_m) as the average of the vertices. Let $a_0 = \frac{w_{0,0} - w_{k,0}}{k}$. Then $a_m = a_0 + \frac{(k-2)}{3(k-1)}h_T$ if $R_{1,0} = \emptyset$ and $a_0 + \frac{(k-2)}{4(k-1)}(h_T + h_t)$ otherwise. If $k = 2$, then this again reduces to $\frac{1}{2}(w_{0,0} - w_{k,0})$. Likewise, $c_m = \frac{1}{3}(\delta_1(k, 0) + \delta_1(0, 0) + 2\delta_1(1, j))$ in the first case and $\frac{1}{2}(\delta_1(1, 0) + \delta_1(1, j))$ in the second.

Finally, we note that to generalize these equations to arbitrary $b_0 \neq 0$, the (weighted) differences in the y terms, that is in the total number of unpaired bases over all junctions between neighboring configurations, would be added to the residual energy differences.

3.3. Datasets. Results are based on analyzing a number of different sets of RNA sequences. They are broadly grouped into three categories:

- (1) the 100 biological ones used in previous studies Poznanović et al. (2020, 2021),
- (2) a total of 24,000 random counterparts for those 100 sequences, and
- (3) the $\sim 4,000$ biological sequences in the Archive II benchmarking dataset Sloma and Mathews (2016); Mathews (2019).

The target region geometry analysis uses the first two categories of sequences. The first dataset, denoted here as the *bio* sequences, are the 50 tRNA and 50 5S rRNA whose full branching polytopes were previously computed and extensively analyzed Poznanović et al. (2020, 2021). These sequences, and their associated secondary structures, were originally selected from the Comparative RNA Web (CRW) Site Cannone et al. (2002) so that their T99 MFE prediction accuracies spanned the full range. Differences in GC content were used to ensure that sequences with similar MFE values generate a diverse set. These 100 sequences, along with comparative secondary structures and some associated details, can be accessed online via <https://github.com/gtDMMB/Datasets>. To assess biological significance, their target region properties were compared against random sequences.

The random counterparts for these bio sequences were generated in three different ways. The primary comparison set, denoted as the *shuf* data, was generated using the *ushuffle* program Jiang et al. (2008). These shuffles are organized into 6 subsets listed in Table 1. Each subset is defined by a relevant sequence characteristic, described in the table caption. For each characteristic, the sequences from each family with the minimum, median, and maximum values were used. In the event of a repeat, the next closest sequence was chosen.

For each of the 18 sequences chosen per family, 500 distinct shuffles were generated preserving dinucleotides/2mers, i.e. length two substrings. The number was based on the formula $n = (z \times s/e)^2$ for the sample size necessary to estimate the mean of a distribution, where s is the initial standard deviation, z is the z-score corresponding to desired confidence level, and e is the margin of error. Based on preliminary data, now included in the mers dataset described below, it was determined that 500 samples would be sufficient for $z = 1.96$ (i.e. 95%) and $e = 0.3$.

To better understand the effect of sequence length, a uniformly random dataset (*unif*) was considered where the probability of each nucleotide is 0.25. A set of 1500 sequences was generated with length 74 for tRNA comparisons, and 121 for the 5S rRNA.

We also consider the effect of *kmer* length by computing a dataset (*mers*) of 1500 sequences split evenly between 2mer, 3mer, and 4mer preserving shuffles of an *Oryza nivara* tRNA sequence and also of the 5S rRNA from *Escherichia coli*.

| tRNA (min/med/max) | | | | | | |
|-----------------------|------------|---------|-----------|--------|-----------|--------|
| eng | CP000493 | -48.00 | AY934351 | -32.30 | AY934184 | -23.00 |
| area | AY934254 | 0 | CP000471 | 59.34 | AP006618 | 160.70 |
| f1 | AY934387_a | 0.2439 | BX569691 | 0.7727 | AE000657 | 1 |
| nntm | AE013169* | 0.0513 | CP000473* | 0.5275 | AE008623 | 1 |
| gc | X04465 | 0.4054 | DQ396875 | 0.5890 | AE014184 | 0.7297 |
| diff | BA000021* | -0.1027 | DQ093144* | 0.0357 | CP000143* | 0.7497 |
| 5S rRNA (min/med/max) | | | | | | |
| eng | M21086 | -102.00 | X13037 | -51.60 | X06094 | -43.00 |
| area | Z75742 | 0 | K02343 | 71.33 | X07545 | 191.17 |
| f1 | V00647 | 0.1579 | M36188* | 0.7671 | X02627 | 0.9167 |
| nntm | M24954* | 0.1714 | M26976 | 0.7294 | AE009942* | 0.8941 |
| gc | U39694 | 0.4322 | X13035 | 0.5750 | X07692* | 0.7165 |
| diff | Z33604 | -0.2724 | X06996 | 0.0001 | X72588 | 0.6788 |

TABLE 1. Accession number and characteristic value for the bio sequences used as the basis for the shuf subsets. Six sequence characteristics were considered. Three were properties of the target region: the residual free energy w from the branching signature (*eng*), the total area (*area*), and the F1-accuracy of the corresponding secondary structure (*f1*). The others were the MFE prediction accuracy (*nntm*) and GC content (*gc*) originally used for sequence selection, as well as the accuracy improvement over that MFE prediction for the target region structure (*diff*). * denotes the replacement for a repeated sequence.

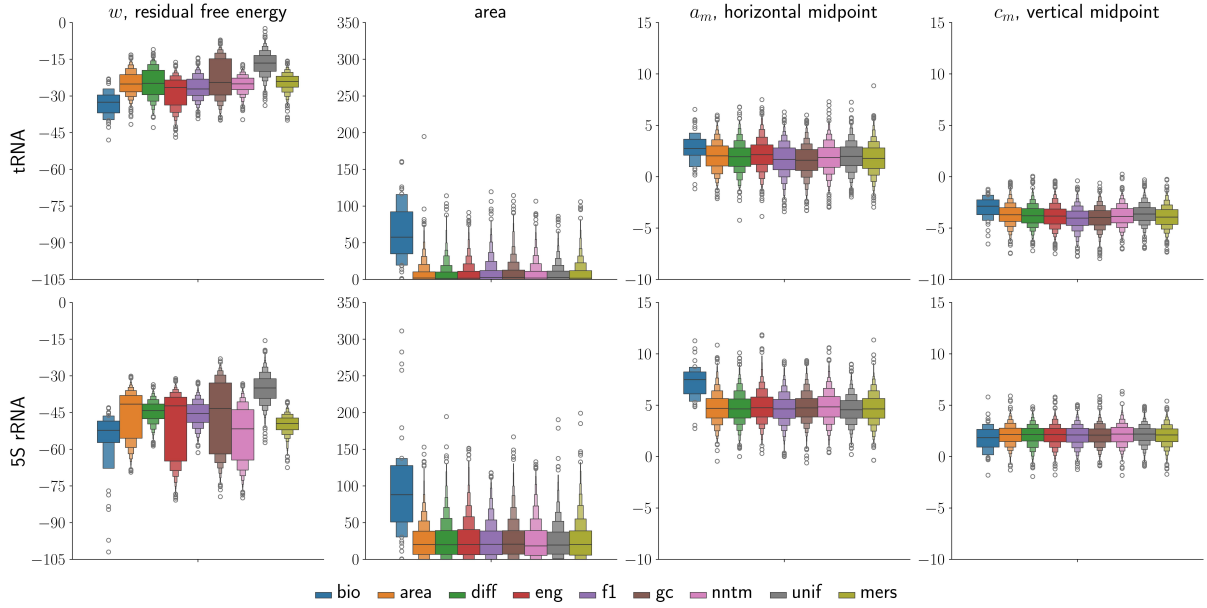


FIGURE 4. Boxen plots Hofmann et al. (2017) for the residual free energy (w), area, and center coordinates (a_m, c_m) in the (\bar{a}, c) -slice, as computed by **SageMath**, for the tRNA and 5S rRNA target regions of $R_{1,1}$ and $R_{1,0}$ respectively. The central box displays the median and interquartile range, as in a standard boxplot. Subsequent boxes cover a similar range to the boxplot whiskers but display more information. The width of the box is exponentially correlated with the percentile shown.

As a consequence of the geometric analysis, we proposed considering alternative predictions generated by varying the branching parameters. To validate the potential accuracy improvements from this approach, it was tested on the Archive II benchmarking dataset Sloma and Mathews (2016); Mathews (2019). This sequence collection was assembled by the Mathews Lab (U Rochester) and is available⁵ online. It consists of sequences from 10 families: 557 tRNA, 1283 5s rRNA, 928 signal recognition particle (SRP) RNA, 454 RNase P, 462 tmRNA, 4 domains each from 22 small subunit ribosomal RNA (16S dom), 98 group I self-splicing introns (grp I intr), 37 telomerase RNA, 6 domains each from 5 large subunit ribosomal RNA (23S dom), and 11 group II self-splicing introns (grp II intr). The 3 tRNA and 33 5S rRNA which happened to coincide with our training set were removed to ensure independence of the testing dataset.

4. RESULTS

The data analysis was evenly split between tRNA and 5S rRNA sequences. For each family, we considered properties of 50 biological sequences against a large set of random comparisons. Most were generated under permutations which preserve the dinucleotide/2mer distribution. Additional randomized comparisons were made to test for dependencies on sequence length and choice of k mer. In total, normal fan slices for 12,000 random sequences were analyzed for each family, grouped into the shuf (75%), unif (12.5%), and mers (12.5%) datasets described in Section 3.3. This was feasible using the new reduced polytope algorithm, but still required more than 1,500 hours of compute time.

4.1. Target region geometry. From Figure 3 in Section 3.2, we see that the size and location of the target regions can be similar within a family but quite different between them. Figure 4 shows that this consistency holds for the randomized data, while also highlighting the very large differences in region area between the bio sequences and their random counterparts.

To begin, we see different w distributions between sequences of similar lengths, i.e. ~ 74 nt for tRNA and ~ 121 nt for 5S rRNA. This is especially true when the randomized comparisons are based on a characteristic, like GC content, which is known to be correlated with thermodynamic stability.

Nonetheless, these differences resolve into consistent geometric properties. Hence, comparing the medians of the 8 random subsets considered, the average (with standard deviation) for the $R_{1,1}$ properties is 2.19 (0.40) for the area with horizontal and vertical center coordinates of 1.89 (0.17) and -3.84 (0.12).

⁵<https://rna.urmc.rochester.edu/publications.html>

| family | reg | \hat{p} | k | p_v | reg | \hat{p} | k | p_v |
|---------|-----|-----------|-----|---------------|-----|-----------|-----|---------------|
| tRNA | 1,0 | 0.9088 | 45 | 0.8042 | 1,1 | 0.6239 | 49 | 0.0000 |
| 5S rRNA | 1,0 | 0.8572 | 49 | 0.0075 | 1,1 | 0.5459 | 16 | 0.0016 |

TABLE 2. P-values for $R_{1,0}$ and $R_{1,1}$ counts for the bio sequences compared to their shuf counterparts under (exact) binomial test. Bold denotes significance at $\alpha = 0.05$ under a Bonferroni correction.

The corresponding ones for $R_{1,0}$ are an area of 19.99 (0.66) centered on 4.70 (0.08) horizontally and 2.15 (0.04) vertically. The upper bound imposed on $R_{1,0}$ is $c_0 = 6.6$ since $\max\{\delta_0(1, j)\} = 6.5$ over the entire dataset.

In contrast, the median bio area is 57.67 for tRNA $R_{1,1}$ and 88.115 for 5S rRNA $R_{1,0}$, and the respective center coordinates are (2.75, -2.86) and (7.5, 1.85). Hence, the biological sequences have significantly different areas overall, irrespective of the choice of comparison subset. The tRNA centers are typically located slightly to the right and somewhat above their randomized counterparts. In contrast, the 5S rRNA ones are shifted noticeably to the right, but barely down. To understand how, and therefore why, this is happening, we use the geometric approximations introduced in Section 3.2, conditioned on region existence.

4.2. Existence and boundary composition. Of the 50 bio sequences for each family, 98% have a target region in the $(a, 0, c, 1)$ -plane. When the other region also exists, they form a boundary so we consider these counts too.

We compare these proportions to the 9000 shuf sequences per family using a binomial test. More precisely, the existence of a particular region is a random variable with estimated probability \hat{p} . The p-value, denoted p_v , for the number of k successes in $n = 50$ trials is reported in Table 2 under a two-tailed test. Significance for this, and for each of the two sets of boundaries considered below, was assessed at $\alpha = 0.05$ under a Bonferroni correction.

The existence of an $R_{1,0}$ is common, but the higher number for 5S rRNA is significant. As we will see, the stability of this region affects the existence of an $R_{1,1}$, so there are significantly fewer than expected. The dual is not observed for tRNA since $R_{1,0}$ is an infinite region. Hence, although the tRNA $R_{1,1}$ p-value is extreme (2.877×10^{-9}), the number of $R_{1,0}$ is typical.

We note that the estimated probabilities between the two families are different. We confirmed (under an ANOVA followed by a Tukey HSD post-hoc test against values for the unif dataset) that this is statistically significant and consistent with the increase in sequence length.

The right boundary of the target regions is always $R_{0,0}$, an infinite region which exists for every sequence. Moreover, there is no significant effect of the target region stability on its left boundary composition, as assessed by comparable binomial tests conditioned on the target. All tRNA $R_{1,1}$ and 79.6% of 5S $R_{1,0}$ are bounded by $R_{2,0}$ on the left, but this is not unusual (\hat{p} , $p_v = 0.9421$, 0.1164 and 0.8394, 0.4341). Nor is that 89.8% of tRNA $R_{1,1}$ are bounded above by $R_{1,0}$ (\hat{p} , $p_v = 0.8937$, 0.8980). However, the bottom boundaries are both significantly different.

Of the 49 tRNA $R_{1,1}$, 42 are bounded below by $R_{1,2}$ and the rest by $R_{1,3}$ (\hat{p} , $p_v = 0.5777$, 0.0000 and 0.3147, 0.0084). Of the 5S rRNA, 16 are bounded below by $R_{1,1}$ and 23 more by $R_{1,2}$ (\hat{p} , $p_v = 0.5331$, 0.0040 and 0.2666, 0.0030). The lower boundaries for the corresponding shuffles range beyond $R_{1,6}$ (for one $R_{1,1}$ and 14 $R_{1,0}$).

We note that if the number which are bounded by the first two regions is instead considered, then the tRNA counts are still significant (\hat{p} , $p_v = 0.8924$, 0.0087) whereas the 5S rRNA are not (\hat{p} , $p_v = 0.7997$, 1). Hence the $R_{1,1}$ lower boundary for biological tRNA sequences is more likely to have a lower degree of branching than expected, whereas this is not the case for $R_{1,0}$ and 5S rRNA. However, the balance between $R_{1,1}$ and $R_{1,2}$ is very unusual for 5S rRNA, most likely due to its $R_{1,0}$ stability.

4.3. Residual energies and their differences. The geometry approximations derived in Section 3.2.2 are determined by the signatures of the surrounding regions. The slope of the boundary lines is a function of the reduced signature variables, but the location (i.e. the axes intercepts) depends on differences in the residual energy w .

As illustrated in Figure 5, there is a range of w terms for individual bio regions. For example, the average and standard deviation for $w_{0,0}$ is (-27.38, 5.37) for tRNA and (-43.13, 10.19) for 5S rRNA yet the difference with their target regions' residual energy is (5.78, 2.94) and (12.93, 4.19) respectively. This is due to the very strong correlation between the w terms in adjacent regions. Figure 5 illustrates

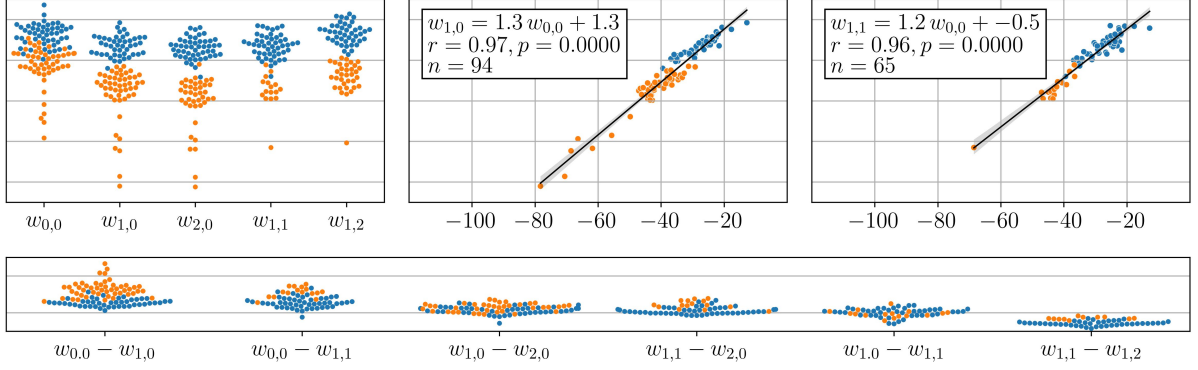


FIGURE 5. Residual energies for the biological tRNA (blue) and 5S rRNA (orange) sequences. Horizontal (grey) lines are at 20 kcal/mol increments. The best line fit was calculated with `scipy.stats.linregress` with Pearson correlation coefficient r and p-value p under the Wald Test.

| family | boundary | b-avg | b-std | s-avg | s-std | p-value | z-avg | z-std |
|---------|------------------|---------|--------|---------|--------|---------------|---------|--------|
| tRNA | $\delta_1(k, 0)$ | -0.5765 | 0.9384 | -1.4254 | 0.8704 | 0.0000 | 0.9752 | 1.0781 |
| | $\delta_1(0, 0)$ | 2.7827 | 1.4532 | 0.5449 | 1.3337 | 0.0000 | 1.6778 | 1.0896 |
| | $\delta_1(1, j)$ | -5.8082 | 1.1974 | -4.8590 | 1.2198 | 0.0000 | 0.7781 | 0.9817 |
| | $\delta_1(1, 0)$ | 0.2932 | 2.3240 | -2.7826 | 1.4595 | 0.0000 | 2.1074 | 1.5923 |
| 5S rRNA | $\delta_0(k, 0)$ | 2.6497 | 2.1185 | 3.1197 | 1.6437 | 0.0465 | -0.2860 | 1.2889 |
| | $\delta_0(0, 0)$ | 12.9286 | 4.2380 | 6.6163 | 2.1807 | 0.0000 | 2.8946 | 1.9434 |
| | $\delta_0(1, j)$ | -2.2081 | 2.1011 | -1.8930 | 1.4544 | 0.1319 | -0.2167 | 1.4447 |

TABLE 3. Energy difference comparison for target region boundaries. P-values were computed under an unpaired Student t-test on the bio (b) and shuf (s) distributions, and bolded when significant at $\alpha = 0.05$ under a Bonferroni correction. The bio z-score summary statistics are also given.

two such correlations for the most dispersed of the six differences pictured; the other correlations are even higher.

We tested whether the strength of these correlations is significant by generating 10,000 random subsets of size 100 (split evenly between the two families) from the shuf dataset for each of the six residual energy differences pictured. For each subset, the Pearson correlation coefficient r was computed, generating an average and standard deviation for the entire dataset against which the bio r values were compared using a z-score. Five out of the six z-scores were negative, and three significantly so (at $\alpha = 0.05$ under a Bonferroni correction) whereas the one positive one, for $w_{1,0}$ versus $w_{2,0}$, was not ($p_v = 0.2668$). Hence, the existence of a strong correlation between neighboring residual energy values is not biologically meaningful.

However, the differences in those energy values can be significant. Recall that the left and bottom boundary regions of the targets are denoted $R_{k,0}$ and $R_{1,j}$, and that the right boundary is always $R_{0,0}$. As discussed in Section 4.2, the k and j values are quite consistent for the bio sequences but can be more variable for the shuf ones. This is factored into the geometric approximations by the weighting on the residual energy differences.

Table 3 summarizes the differences between the bio and shuf distributions. We see that the 5S rRNA $R_{1,0}$ lower and left boundaries are not significantly different from random, but all the others are strongly so.

To further quantify this, the z-score of each bio sequence was computed, and summary statistics are also reported. An ANOVA, followed by a Tukey HSD post-hoc test, on the tRNA z-scores and on the 5S ones confirms that the difference among boundaries is significant (both $p_v = 0.0000$) but that the differences between $R_{k,0}$ and $R_{1,j}$ in both families are not ($p_v = 0.8474$ and 0.9744). Moreover, neither are the differences between the top and right boundaries for tRNA ($p_v = 0.3123$).

Hence, we conclude that essentially all the geometric difference for 5S rRNA is due to the relative stability of the (1,0) region over the (0,0) one. While this boundary, along with the top one, is also a major factor for tRNA, the left and bottom boundaries are a significant contribution as well.

4.4. Geometric consequences. First, we consider how well the geometric formula approximate the area of the target regions. Recall that any difference is caused by additional boundaries in the lower left corner. These decrease the actual area, and consequently shift the center coordinates. Relatively few of the $R_{1,0}$ are affected in this way. Of the 10,314 considered, 72.66% have an absolute error in the area approximation < 0.1 and only 9.5% are > 1 . Only 7 are > 10 , and the maximum is 19.0638. The formula are also a very good approximation for the tRNA $R_{1,1}$, although their boundaries can be more complex. More than half (52%) of the 7570 considered have an absolute error < 0.1 , with only 22.5% being > 1 , 53 being > 10 and a maximum of 26.2825. Hence, the conclusions drawn from the residual energy comparisons just considered are determining factors in the large differences in area observed.

In particular, the size of the $R_{1,0}$ target region for 5S rRNA is driven by its stability relative to $R_{0,0}$. This results in a much larger width, but no meaningful difference in height. As a consequence, the center is shifted horizontally, but not vertically. Yet, the existence of an $R_{1,1}$ was found to be significantly different for the bio sequences.

To gain some insight, the $\delta_0(1, j)$ values were considered only for those bio and shuf sequences with $j > 1$. These were compared with the 5S rRNA $\delta_1(1, j)$ values for bio and shuf datasets. An ANOVA followed by a Tukey HSD post-hoc test found that the two shuf distributions are significantly different ($p_v = 0.0000$) from each other but the two bio ones are not ($p_v = 0.9978$). Hence, for the bio sequences but not the shuf ones, the $R_{1,0}$ bottom when $j > 1$ is very close to where the $R_{1,1}$ bottom is likely to have been. Moreover, the bio $\delta_0(1, j)$ value when $j = 1$ is significantly higher (-0.4313 versus -3.0695, $p_v = 0.0000$) than not. Thus, more 5S rRNA do not have a $R_{1,1}$ than expected.

In contrast, all four boundaries contribute to the size of the tRNA $R_{1,1}$. As a consequence the effect on the center location is less pronounced, although it is shifted right and up, consistent with the greater contributions of $\delta_1(0, 0)$ and $\delta_1(1, 0)$ than $\delta_1(k, 0)$ and $\delta_1(1, j)$. Due to the slope of the boundary lines, the width is closely related to the “full” triangle height $h_T = \delta_1(0, 0) + \delta_1(k, 0) - \delta_1(1, j)$. We find, though, that the distribution of h_t is quite similar to the random ones. In other words, the stability of $R_{1,1}$ relative to $R_{1,0}$ results in essentially the same amount being deducted from the full triangle area as for the random sequences when $R_{1,0}$ exists. This is consistent with the tRNA $R_{1,0}$ being like their random counterparts.

4.5. Prediction. Previous work Poznanović et al. (2020) demonstrated that understanding the polytope geometry can help improve predictions under NNTM optimization. The ad-hoc parameters determined by analyzing intersections of regions of interest for our 100 tRNA and 5S rRNA sequences showed improved accuracy across both families. However, since we also considered families separately, we observed that the combined accuracy was well below what could be achieved with family-specific parameters.

Subsequent development of a branch-and-bound algorithm Poznanović et al. (2021) to assess potential improvements across families confirmed that the ad-hoc parameters performed as well as it could be expected. Both ad-hoc and branch-and-bound parameters led to improved predictions on a larger testing set of tRNA and 5S rRNA sequences from the Archive II dataset Sloma and Mathews (2016); Mathews (2019), with ad-hoc parameters outperforming, likely due to reduced overfitting to the training data.

Here, we adopt the same approach used in Poznanović et al. (2020) to identify the ad-hoc parameters. We construct the graph of pairwise intersections of target regions across the entire training set of 100 sequences, as well as each family separately. In this graph, two regions are connected if they intersect. We then identify maximal cliques and take cumulative intersections over those cliques. The aim is to find a single parameter combination, but we consider each family separately in order to develop understanding how the accuracy of each is affected by inclusion of the other in the training set. As suggested by the example in Figure 3, pairwise intersections across families are easily found. The problem is that their locations vary, making finding cumulative intersections of multiple regions more challenging.

Each family was found to have only a few maximal cliques, each with a nonempty intersection. Moreover, for each family we identified a large “core” which belongs to all maximal cliques containing over 80% of the sequences. As illustrated in Figure 6, the core intersections of tRNA and 5S rRNA are distinctly separated, even exhibiting opposite preferences for the sign of the c -parameter.

In contrast, the entire set’s intersection graph contained numerous maximal cliques of varying sizes, with most cumulative intersections being empty. The largest subsets with nonempty intersections include only about two-thirds of the sequences and some of them are skewed toward tRNA. The cumulative intersection for the most balanced clique between families (Figure 6) is small and disjoint from both core intersections. Therefore, while each family’s prediction can be improved with different parameter sets, using a single parameter set results in lower accuracy than family-specific parameters.

Given the evidence that the best linear approximation of the branching term varies between families, we suggest considering optimal structures under multiple linear approximations as a basis for predictions,

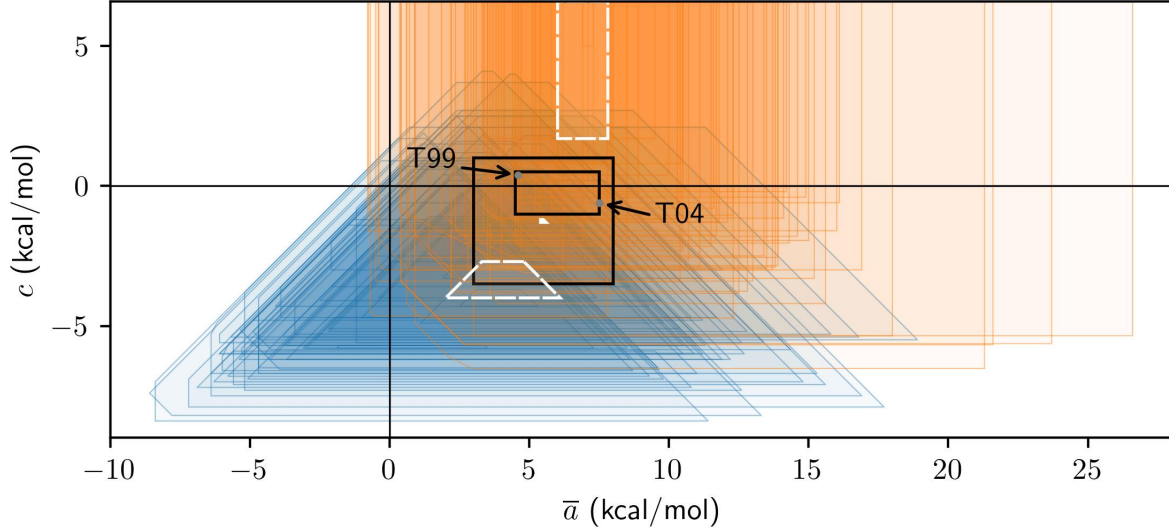


FIGURE 6. The target regions for tRNA (blue trapezoids) are overlayed with those for 5S rRNA (orange rectangles). Regions with white boundaries represent the cumulative intersections of the target regions for a large core identified within each family, as well as the most balanced clique across families – 42 tRNA (bottom), 44 5S rRNA (top) and 31 tRNA and 35 5S rRNA (middle). The search rectangles Trec (smaller) and Grec (larger) are shown in black, with the unskewed versions of the T99 and T04 parameters marked inside. The precise region locations are as follows. tRNA : vertices $(4.8, -2.7)$, $(3.3, -2.7)$, $(2.0, -4.0)$, $(6.1, -4.0)$, 5S rRNA: $6 \leq \bar{a} \leq 7.8$, $c \geq 1.7$, tRNA/5S rRNA: vertices $(5.4, -1.3)$, $(5.4, -1.2)$, $(5.5, -1.2)$, $(5.6, -1.3)$, Trec: $4.5 \leq \bar{a} \leq 7.5$, $-1 \leq c \leq 0.5$, Grec: $3 \leq \bar{a} \leq 8$, $-3.5 \leq c \leq 1$.

rather than choosing a single parameter set. We test this idea on the Archive II dataset, sampling parameters from two rectangles in 0.5 increments. The first rectangle we consider (Trec) is the smallest rectangle containing the T99 and T04 (unskewed) parameters, while the second rectangle (Grec) was selected based on the geometry of the 100 target regions in our training set. Bounds for the \bar{a} values were chosen based on the ranges of the \bar{a} values of the centers of the target regions in both families and is not much bigger than the Trec \bar{a} range. Since the 5S RNA regions are infinite vertical strips, with the tRNA trapezoidal regions being generally lower than them, the c range was chosen based on the top decile of the bottom boundaries for 5S RNA and the bottom decile of the top boundaries for tRNA, rounded to the nearest 0.5 increment and expanded to include an extra row.

Table 4 shows significant improvements in prediction accuracy when, instead of using only T04, multiple structures optimal under branching parameters from Trec are considered. We report accuracy for each family separately because the test data is highly unbalanced. We observe that the number of structures generated generally remains within single digits for the sequence lengths in our test set. Further improvements were observed when sampling from Grec (significant under a Bonferroni correction) for all families except the group II intron, likely due to sample size. Improvements for tRNA and 5S rRNA sequences from the Archive II data indicate that we are not overfitting to our training sequences when considering the larger rectangle.

Based on the existence of a much better prediction in a not much bigger set of structures, this is a promising new way for sampling structures for prediction. We discuss possible directions in which this method can be developed to generate a prediction in the Conclusions section.

5. DISCUSSION

Previous analysis of branching parameters which improve the MFE prediction indicated that different parameter combinations favor different families. Here we focused on the two families which were analyzed previously – tRNA and 5S rRNA – and on the regions made of the parameters which yield the same optimal structure for each RNA sequence, rather than parameter combinations.

When compared to their dinucleotide shuffles, the existence of the target branching region is observed more frequently for the biological sequences. We find statistically that the region existence is partly

| sequences | | | T04 | Trec | | | Grec | | |
|-------------|------------|-------------|------|------|-------------------|-------------------------------|------|--------------------|-------------------------------|
| family | seq len | set size | acc | acc | p-value vs T04 | structures (avg \pm std) | acc | p-value vs Trec | structures (avg \pm std) |
| tRNA* | 77 | 555 | 0.53 | 0.68 | 0.0000 | 2 ± 1 | 0.79 | 0.0000 | 3 ± 1 |
| 5S rRNA* | 119 | 1250 | 0.62 | 0.66 | 0.0000 | 2 ± 1 | 0.68 | 0.0000 | 4 ± 2 |
| SRP | 184 | 928 | 0.67 | 0.69 | 0.0000 | 2 ± 1 | 0.70 | 0.0000 | 5 ± 4 |
| RNaseP | 332 | 454 | 0.52 | 0.61 | 0.0000 | 5 ± 2 | 0.66 | 0.0000 | 17 ± 5 |
| tmRNA | 366 | 462 | 0.40 | 0.49 | 0.0000 | 6 ± 2 | 0.53 | 0.0000 | 17 ± 5 |
| 16S dom | 378 | 88 | 0.53 | 0.59 | 0.0000 | 4 ± 3 | 0.61 | 0.0001 | 15 ± 9 |
| grp I intr | 426 | 98 | 0.51 | 0.57 | 0.0000 | 6 ± 3 | 0.61 | 0.0000 | 20 ± 4 |
| telomerase | 445 | 37 | 0.49 | 0.55 | 0.0000 | 5 ± 2 | 0.58 | 0.0013 | 16 ± 4 |
| 23S dom | 461 | 30 | 0.66 | 0.73 | 0.0008 | 6 ± 3 | 0.76 | 0.0032 | 19 ± 9 |
| grp II intr | 717 | 11 | 0.28 | 0.34 | 0.0003 | 11 ± 3 | 0.37 | 0.0417 | 37 ± 8 |

TABLE 4. Per family prediction accuracy on the Archive II data set (*the tRNA and 5S rRNA sequences which happened to coincide with the training set were excluded from the test set). The first three columns describe the composition of the data set. Comparisons are given between the average accuracy (*acc*) of the optimal structure under the T04 parameters (measured as the F1-score) and the most accurate structure found within the Trec rectangle, as well as the best structures within the extended Grec rectangle. The p-value from a paired t-test is given for each family and bolded when significant at $\alpha = 0.05$ under a Bonferroni correction. The number of different structures seems to grow linearly with sequence length.

affected by sequence length and it would be interesting to find a mathematical explanation for this fact. However, we find that this does not explain the differences for the biological sequences – they have the target region more frequently than expected for their length.

To analyze the geometry of the target regions for these families, it is useful to perform a change of variables and consider only the excess instead of the total amount of branching in the secondary structure. While this formulation cannot be used directly in the optimization since it is not amenable to subdivision, it eliminates the 1/3 skew in the original parameter space and makes the regions more symmetric. The transformation is invertible, so any conclusion obtained about the parameters in the unskewed space translates directly to an analogous one for the original parametrization.

We give a geometric description of the target branching regions for tRNA and 5S rRNA and we show that they are well approximated by a triangle or trapezoid (for tRNA) and an infinite vertical strip (for 5S rRNA). The formulas we derive imply that the region location and boundaries depend on the relative difference between the residual energies of the target branching structure and only 3 or 4 other branching patterns.

While the geometry of the target region is intrinsic to the NNTM optimization, its size is due to the biological signal. It is known that functional RNAs have lower folding energy than random RNAs of the same length and dinucleotide frequency Clote et al. (2005). However, the residual energies for different regions are correlated, so this fact does not imply difference in the regions of different biological and random sequences. Interestingly, the statistical analysis of the residual differences (due to the stackings and other loops) of the target and neighboring structures for tRNA and 5S rRNA showed that the distributions are similar for each family and are a new type of biological signal. This explains why the target regions within each family have a large overlap and why we can improve the prediction for each family separately.

We also showed that while the overlap of the target regions across families is smaller than within each family, the location we observe for tRNA and 5S rRNA indicates an area which might be useful for other families of sequences, if one is open to considering other possible optimal structures by varying the branching parameters. With the rectangle search, the prediction improved for all of the families in the testing set, while the set of structures generated wasn’t very large and appeared to grow linearly with sequence length. It might be of interest to be able to consider only the proposed search rectangle here or to further “zoom into” a related area.

6. CONCLUSIONS

This work answers open questions while raising new ones. We now understand why multiple parameter optimization approaches have concluded that it is impossible to improve predictions for both tRNA and

5S rRNA simultaneously Ward et al. (2017); Poznanović et al. (2020). Significant improvements for both families are achievable, but only for different parameters, and as previous work has shown Poznanović et al. (2021), this disparity is not due to either family being an outlier. Some of the other families in the Archive II set show improved predictions with tRNA-like parameters, while others benefit more from 5S rRNA-like parameters.

As we observed, substantial gains in accuracy can be achieved by considering multiple branching configurations. This approach suggests a new direction to explore for improving NNTM optimization. It also raises a key question: how should we handle the structures generated? Multiple approaches such as summarizing the data Ding and Lawrence (2001); Rogers and Heitsch (2014), re-evaluating under more sophisticated energy models Liu et al. (2011); Zuber and Mathews (2024), or incorporating chemical footprinting data Ge and Zhang (2015) have been successfully applied in other prediction methods that rely on large samples, making them natural next steps to explore.

To generate the data, we developed an algorithm for generating a fixed $b = b_0, d = 1$ slice of the normal fan of the branching polytope for each sequence. The algorithm is faster than considering the whole branching polytope, as it effectively disregards a large proportion of secondary structures which do not correspond to the parameters in the slice of interest. While effective for our calculations, its complexity remains prohibitive for practical use for longer RNA sequences. Therefore, it would be advantageous to develop an algorithm that generates only a part of the slice, which would further speed up the computations by excluding a significant number of irrelevant structures for longer sequences. We plan to pursue this in future work.

REFERENCES

- Tinoco, Jr, I., Bustamante, C.: How RNA folds. *J Mol Biol* **293**(2), 271–281 (1999)
- Miao, Z., Adamiak, R.W., Antczak, M., Boniecki, M.J., Bujnicki, J., Chen, S.-J., Cheng, C.Y., Cheng, Y., Chou, F.-C., Das, R., Dokholyan, N.V., Ding, F., Geniesse, C., Jiang, Y., Joshi, A., Krokhotin, A., Magnus, M., Mailhot, O., Major, F., Mann, T.H., Piątkowski, P., Pluta, R., Popena, M., Sarzynska, J., Sun, L., Szachniuk, M., Tian, S., Wang, J., Wang, J., Watkins, A.M., Wiedemann, J., Xiao, Y., Xu, X., Yesselman, J.D., Zhang, D., Zhang, Y., Zhang, Z., Zhao, C., Zhao, P., Zhou, Y., Zok, T., Żyła, A., Ren, A., Batey, R.T., Golden, B.L., Huang, L., Lilley, D.M., Liu, Y., Patel, D.J., Westhof, E.: RNA-Puzzles Round IV: 3D structure predictions of four ribozymes and two aptamers. *RNA* **26**(8), 982–995 (2020)
- Schneider, B., Sweeney, B.A., Bateman, A., Cerny, J., Zok, T., Szachniuk, M.: When will RNA get its Alphafold moment? *Nucleic Acids Res* **51**(18), 9522–9532 (2023)
- Nithin, C., Kmiecik, S., Błaszczuk, R., Nowicka, J., Tuszyńska, I.: Comparative analysis of RNA 3D structure prediction methods: towards enhanced modeling of RNA–ligand interactions. *Nucleic Acids Res* **52**(13), 7465–7486 (2024)
- Markham, N.R., Zuker, M.: UNAFold: software for nucleic acid folding and hybridization. *Methods Mol Biol* **453**, 3–31 (2008)
- Lorenz, R., Bernhart, S.H., Siederdisen, C., Tafer, H., Flamm, C., Stadler, P.F., Hofacker, I.L.: ViennaRNA Package 2.0. *Algorithms Mol Biol* **6**(26) (2011)
- Reuter, J.S., Mathews, D.H.: RNAstructure: software for RNA secondary structure prediction and analysis. *BMC bioinformatics* **11**(129) (2010)
- Mathews, D.H.: Revolutions in RNA secondary structure prediction. *J Mol Biol* **359**(3), 526–32 (2006)
- Rogers, E., Heitsch, C.: New insights from cluster analysis methods for RNA secondary structure prediction. *Wiley Interdiscip Rev RNA* **7**(3), 278–94 (2016)
- Jaeger, J.A., Turner, D.H., Zuker, M.: Improved predictions of secondary structures for RNA. *Proc Natl Acad Sci U S A* **86**(20), 7706–10 (1989)
- Mathews, D.H., Sabina, J., Zuker, M., Turner, D.H.: Expanded sequence dependence of thermodynamic parameters improves prediction of RNA secondary structure. *J Mol Biol* **288**(5), 911–940 (1999)
- Mathews, D.H., Disney, M.D., Childs, J.L., Schroeder, S.J., Zuker, M., Turner, D.H.: Incorporating chemical modification constraints into a dynamic programming algorithm for prediction of RNA secondary structure. *Proc Natl Acad Sci U S A* **101**(19), 7287–7292 (2004)
- McCaskill, J.S.: The equilibrium partition function and base pair binding probabilities for RNA secondary structure. *Biopolymers* **29**(6-7), 1105–19 (1990)
- Ding, Y., Lawrence, C.E.: A statistical sampling algorithm for RNA secondary structure prediction. *Nucleic Acids Res* **31**(24), 7280–7301 (2003)
- Zuker, M.: On finding all suboptimal foldings of an RNA molecule. *Science* **244**(4900), 48–52 (1989)

- Wuchty, S., Fontana, W., Hofacker, I.L., Schuster, P.: Complete suboptimal folding of RNA and the stability of secondary structures. *Biopolymers* **49**(2), 145–65 (1999)
- Entzian, G., Hofacker, I.L., Ponty, Y., Lorenz, R., Tanzer, A.: RNAXplorer: harnessing the power of guiding potentials to sample RNA landscapes. *Bioinformatics* **37**(15), 2126–2133 (2021)
- Drellich, E., Gainer-Dewar, A., Harrington, H., He, Q., Heitsch, C.E., Poznanović, S.: Geometric combinatorics and computational molecular biology: Branching polytopes for RNA sequences. In: Heather A. Harrington, M.W. Mohamed Omar (ed.) *Algebraic and Geometric Methods in Applied Discrete Mathematics*. Contemporary Mathematics, vol. 685, pp. 137–154. American Mathematical Society, Providence, RI, USA (2017)
- Barrera-Cruz, F., Heitsch, C., Poznanović, S.: On the structure of RNA branching polytopes. *SIAM J. Appl. Algebra Geometry* **2**(3), 444–461 (2018)
- Poznanović, S., Barrera-Cruz, F., Kirkpatrick, A., Ielusic, M., Heitsch, C.: The challenge of RNA branching prediction: a parametric analysis of multiloop initiation under thermodynamic optimization. *J Struct Biol* **210**(1), 107475 (2020)
- Poznanović, S., Wood, C., Cloer, M., Heitsch, C.: Improving RNA branching predictions: Advances and limitations. *Genes (Basel)* **12**(4), 469 (2021)
- Turner, D.H., Mathews, D.H.: NNDB: the nearest neighbor parameter database for predicting stability of nucleic acid secondary structure. *Nucleic Acids Res* **38**(suppl_1), 280–282 (2010)
- Sloma, M.F., Mathews, D.H.: Exact calculation of loop formation probability identifies folding motifs in RNA secondary structures. *RNA* **22**(12), 1808–1818 (2016)
- Mathews, D.H.: How to benchmark RNA secondary structure prediction accuracy. *Methods* **162–163**, 60–67 (2019)
- Freier, S.M., Kierzek, R., Jaeger, J.A., Sugimoto, N., Caruthers, M.H., Neilson, T., Turner, D.H.: Improved free-energy parameters for predictions of RNA duplex stability. *Proc Natl Acad Sci U S A* **83**(24), 9373–9377 (1986)
- Xia, T., SantaLucia, Jr, J., Burkard, M.E., Kierzek, R., Schroeder, S.J., Jiao, X., Cox, C., Turner, D.H.: Thermodynamic parameters for an expanded nearest-neighbor model for formation of RNA duplexes with Watson-Crick base pairs. *Biochemistry* **37**(42), 14719–14735 (1998)
- Ward, M., Datta, A., Wise, M., Mathews, D.H.: Advanced multi-loop algorithms for RNA secondary structure prediction reveal that the simplest model is best. *Nucleic Acids Res* **45**(14), 8541–8550 (2017)
- Swenson, M.S., Anderson, J., Ash, A., Gaurav, P., Sükösd, Z., Bader, D.A., Harvey, S.C., Heitsch, C.E.: GTfold: Enabling parallel RNA secondary structure prediction on multi-core desktops. *BMC Res Notes* **5**(1), 341 (2012)
- Diamond, J.M., Turner, D.H., Mathews, D.H.: Thermodynamics of three-way multibranch loops in RNA. *Biochemistry* **40**(23) (2001)
- Mathews, D.H., Turner, D.H.: Experimentally derived nearest-neighbor parameters for the stability of RNA three- and four-way multibranch loops. *Biochemistry* **41**(3), 869–80 (2002)
- Jaeger, J.A., Turner, D.H., Zuker, M.: Improved predictions of secondary structures for RNA. *Proc Natl Acad Sci U S A* **86**(20), 7706–7710 (1989)
- Zuker, M., Mathews, D.H., Turner, D.H.: Algorithms and thermodynamics for RNA secondary structure prediction: A practical guide. In: Barciszewski, J., Clark, B.F.C. (eds.) *RNA Biochemistry and Biotechnology*. NATO ASI Series, pp. 11–43. Kluwer Academic Publishers, Dordrecht, Netherlands (1999)
- Aalberts, D.P., Nandagopal, N.: A two-length-scale polymer theory for RNA loop free energies and helix stacking. *RNA* **16**(7) (2010)
- Huggins, P.: iB4e: A software framework for parametrizing specialized LP problems. In: *Mathematical Software-ICMS 2006: Second International Congress on Mathematical Software*, Castro Urdiales, Spain, September 1–3, 2006. Proceedings 2, pp. 245–247 (2006). Springer
- Grünbaum, B., Klee, V., Perles, M.A., Shephard, G.C.: *Convex Polytopes* vol. 16. Springer, New York, NY (1967)
- The Sage Developers: SageMath, the Sage Mathematics Software System (Version 9.2). (2020). <https://www.sagemath.org>
- Cannone, J.J., Subramanian, S., Schnare, M.N., Collett, J.R., D’Souza, L.M., Du, Y., Feng, B., Lin, N., Madabusi, L.V., Müller, K.M., Pande, N., Shang, Z., Yu, N., Gutell, R.R.: The Comparative RNA Web (CRW) Site: an online database of comparative sequence and structure information for ribosomal, intron, and other RNAs. *BMC Bioinformatics* **3**(1), 2 (2002)
- Jiang, M., Anderson, J., Gillespie, J., Mayne, M.: uShuffle: a useful tool for shuffling biological sequences while preserving the k -let counts. *BMC Bioinformatics* **9** (2008)

- Hofmann, H., Kafadar, K., Wickham, H.: Letter-value plots: Boxplots for large data. *Journal of Computational and Graphical Statistics* **26**(3), 469–477 (2017)
- Clote, P., Ferré, F., Kranakis, E., Krizanc, D.: Structural RNA has lower folding energy than random RNA of the same dinucleotide frequency. *RNA* **11**(5), 578–591 (2005)
- Ding, Y., Lawrence, C.E.: Statistical prediction of single-stranded regions in RNA secondary structure and application to predicting effective antisense target sites and beyond. *Nucleic Acids Res* **29**(5), 1034–1046 (2001)
- Rogers, E., Heitsch, C.E.: Profiling small RNA reveals multimodal substructural signals in a Boltzmann ensemble. *Nucleic Acids Res* **42**(22), 171–171 (2014)
- Liu, B., Diamond, J.M., Mathews, D.H., Turner, D.H.: Fluorescence competition and optical melting measurements of RNA three-way multibranch loops provide a revised model for thermodynamic parameters. *Biochemistry* **50**(5), 640–653 (2011)
- Zuber, J., Mathews, D.H.: Estimating RNA secondary structure folding free energy changes with efn2. In: *RNA Folding: Methods and Protocols*, pp. 1–13. Springer, Clifton, N.J. (2024)
- Ge, P., Zhang, S.: Computational analysis of RNA structures with chemical probing data. *Methods* **79**, 60–66 (2015)

Email address: `spoznan@clemson.edu`

SCHOOL OF MATHEMATICAL AND STATISTICAL SCIENCES, CLEMSON UNIVERSITY, CLEMSON, SC, U.S.A.

Email address: `owencardwell@gatech.edu`

SCHOOL OF MATHEMATICS, GEORGIA INSTITUTE OF TECHNOLOGY, ATLANTA, GA, USA

Email address: `heitsch@math.gatech.edu`

SCHOOL OF MATHEMATICS, GEORGIA INSTITUTE OF TECHNOLOGY, ATLANTA, GA, USA